One-dimensional yttrium silicide electride (Y5Si3:e−) for encapsulation of volatile fission products

Kuganathan, K., Chroneos, A. & Grimes, R.,

Original citation & hyperlink:
Kuganathan, K, Chroneos, A & Grimes, R 2021, 'One-dimensional yttrium silicide electride (Y5Si3:e−) for encapsulation of volatile fission products', Journal of Applied Physics, vol. 129, 245105.
https://dx.doi.org/10.1063/5.0051895

DOI 10.1063/5.0051895
ISSN 0021-8979
ESSN 1089-7550

Publisher: American Institute of Physics

One-dimensional yttrium silicide electride ($Y_5Si_3:e^-$) for encapsulation of volatile fission products

Navaratnarajah Kuganathan[1,2*], Alexander Chroneos[1,2] and Robin W. Grimes[1]

[1]Department of Materials, Imperial College London, London, SW7 2AZ, United Kingdom

[2]Faculty of Engineering, Environment and Computing, Coventry University, Priory Street, Coventry CV15FB, United Kingdom

---

Abstract

Better ways are needed to capture radioactive volatile fission products (Kr, Xe, Br, I, Te, Rb and Cs), discharged during the reprocessing of spent nuclear fuel, in order to reduce volumes of wastes arising and minimise environmental impact. Using density functional theory, we examine the efficacy of a one-dimensional yttrium silicide electride ($Y_5Si_3:e^-$) as a host matrix to encapsulate these species. Endoergic encapsulation energies calculated for Kr, Xe, Rb and Cs imply they are not captured by $Y_5Si_3:e^-$. Encapsulation is exoergic for Br, I and Te with respect to their atoms and dimers as reference states, meaning that they can be captured effectively due to their high electronegativities. This is further supported by the formation of anions due to charge transfer between $Y_5Si_3:e^-$ and Br (I and Te). The selectivity of this material for these volatile species makes it promising for use in nuclear filters.

Keywords: Fission products; electride; $Y_5Si_3:e^-$; DFT; encapsulation energy;

*Corresponding author, e-mail: n.kuganathan@imperial.ac.uk

1. Introduction

Spent nuclear fuel is reprocessed to extract the unused fissile ^{235}U and reduce waste volumes [1-5]. This gives rise to a substantial volume of fission product containing effluent. If fission products can be separated, the effluent can be treated as a lower hazard material. The fission products (Xe, Kr, Br, I, Rb, Cs and Te) are of particular concern as they can escape from the fuel as a consequence of various issues including nuclear power plant accidents and natural crisis. Radioactive iodine (^{131}I) is important because it can be absorbed at high concentration by the human thyroid gland leading to several thyroid disorders [3,6,7]. Radioactive caesium (^{137}Cs) is also of concern as it causes damage to human organs such as kidney and lungs [8-10]. Thus, special provision must be made for the effective and safe disposal of volatile fission products in order to reduce the risk of release.

Impregnated carbon or charcoal filters are most commonly used to trap iodine in nuclear plant [11]. The preference for this type of filter is due to its large trapping surface area and low production cost [11]. Alternative materials such as silica, zeolites, alumina, silver nitrate, metal organic frameworks and porous organic polymers have been examined in order to find a more efficient trapping medium, [12-15]. The efficiency of filters depends upon the properties of the filter material: their thermal and mechanical stability, surface area and chemical species specificity. The search for alternative filter materials continues in order to reduce the potential impact on the environment and human.

Electrides are a class of materials where electrons serve as loosely bound anions [16]. Based on the electron localization, they fall into three categories: zero-dimensional (electrons residing in cavities)[17,18], one-dimensional (electrons in a channel)[19,20] and two-dimensional (electrons localising in a layer)[21]. A zero dimensional "mayenite" type electride, $[Ca_{24}Al_{28}O_{64}]^{4+}\bullet(e^-)_4$, has been widely studied due to its utility as a catalyst for NH_3 synthesis and CO_2 depletion, an electron emitter and superconductor [22-28]. A variety of atoms and molecules have been encapsulated experimentally to examine the effectiveness of encapsulation and studied theoretically to understand how encapsulation modifies the electronic properties of this electride [27-32].

Zhang *et al.* [20] first reported the structure of the apatite based one-dimensional electride $[La_8Sr_2(SiO_4)_6]^{4+}\bullet(e^-)_4$, though its practical utility had not yet been established. An experimental report of the two-dimensional dicalcium nitride electride $[(Ca_2N)^+\bullet e^-]$ by Lee *at al.* [21] shows that this electride is stable at room temperature and exhibits an open layer structure with high electron concentration and a low work function of 2.6 eV. This electride has been tested with regard to application in sodium ion batteries [33] and solid lubricants

[34].

The air and water stable one dimensional electride yttrium silicide ($Y_5Si_3:e^-$) was first reported by Lu *et al.* [35]. This material is a candidate for trapping volatile fission products due to its chemical stability, facilitated by the strong hybridization between yttrium $4d$ electrons and anionic electrons available in the quasi-one-dimensional channels. The number of anionic electrons per formula is predicted to be 0.79 with the effective formula of the electride then described as $[Y_5Si_3]^{0.79+}$: $0.79e^-$ [35]. Ru-loaded $Y_5Si_3:e^-$ is catalytically highly efficient for ammonia synthesis because the anionic electrons enhance the nitrogen cleavage and reduce the associated activation energy [35].

In this study, spin-polarized mode density functional theory (DFT) is used to calculate the structures associated with volatile fission products (Kr, Xe, Br, I, Rb, Cs and Te) encapsulated in $Y_5Si_3:e^-$, their associated encapsulation energies, charge transfer, electronic structures and charge densities.

2. Computational Methods

All calculations were performed using the DFT code VASP (Vienna ab initio Simulation Package) [36]. This code solves standard Kohn-Sham equations using plane wave basis sets and projected augmented wave (PAW) pseudopotentials [37]. In the PAW method, projectors and auxiliary functions are introduced similar to the ultra-soft pseudo potential method and the total energy function includes auxiliary functions. Furthermore, this method keeps the full all-electron wave function as opposed to the other pseudo potential method in which only valence pseudo wave functions are kept. In all calculations, a plane wave basis set with a cut-off of 500 eV and an 4×4×8 Monkhorst-Pack [38] k-point mesh were employed. Further increase in the k-points to 6x6x12 resulted in total energy difference of only 0.8 meV per atom. The exchange-correlation energy was modelled using the generalized gradient approximation (GGA) scheme as defined by Perdew, Burke and Ernzerhof (PBE) [39]. All defect calculations were performed using a 2×2×2 supercell containing 128 atoms (Y:80 and Si:48). the conjugate gradient algorithm [40] was used to perform full geometry optimization (both atom positions and lattice constants were relaxed simultaneously). In all relaxed configurations, forces on the atoms were less than 0.001 eV/Å. The following equation was used to calculate single atom encapsulation energies within $Y_5Si_3:e^-$.

$$E_{Enc} = E_{(X@Y_5Si_3:e^-)} - E_{(Y_5Si_3:e^-)} - E_{(X)}, \quad (1)$$

where $E_{(X@Y_5Si_3:e^-)}$ is the total energy of a single fission atom encapsulated in a 2×2×2 supercell of $Y_5Si_3:e^-$, $E_{(Y_5Si_3:e^-)}$ is the total energy of a 2 ×2×2 supercell of $Y_5Si_3:e^-$ and $E_{(X)}$

is the energy of an isolated gas phase fission atom. A semi empirical dispersion term was used to describe short-range interactions [43].

3. Results and discussion

3.1. Crystal structre of Yttrium silicide

At room temperature yttrium silicide exhibits an hexagonal phase with the space group $P6_3/mcm$ (193), a= b= 8.403, Å, c=6.303 Å, α=β=90° and γ=120° as shown in Figure 1a [41]. There are two non-equivalent Y sites. The first Y site forms three coordination with adjacent Si atoms. The second Y is bonded to six nearest neighbor Si atoms forming a six-coordinate geometry. The crystal structure of $Y_5Si_3:e^-$ was relaxed under constant pressure to obtain equilibrium lattice constants to validate the quality of the basis sets and pseudopotentials. Table 1 reports the calculated lattice parameters together with experimental values: it is evident that there is a good agreement between the calculated and experimental values.

the one-dimensional electron distribution and the total density of states (DOS) plots are shown in Figure 1b and 1c respectively. $Y_5Si_3:e^-$ exhibits metallic behaviour in agreement with a DFT study performed by Lu *et al.*[35]

3.2. Encapsulation of single noble gas atoms (Kr and Xe)

Relaxed structures of $Y_5Si_3:e^-$ with encapsulated Kr and Xe are shown in Figure 2. Endoergic encapsulation energies are calculated for both Kr and Xe inferring their instability within the lattice (see Table 2). The encapsulation energy calculated for Kr is less unfavourable than Xe due to the smaller atomic radius of Kr than Xe [42]. This is further evidenced by the shorter Y-Kr bond length and smaller volume change predicted for Kr (see Table 2). According to Bader charge analysis [43], both noble gas atoms gain a small negative charge (Kr: –0.40 and Xe: –0.48) due to the polarisation between the one-dimensional holes along the *c* axis and the noble gas atoms. The smaller value for Kr reflects the smaller polarizability of Kr.

Total DOS plots predicted for structures with Xe and Kr are almost identical to the DOS plot of encapsulant free $Y_5Si_3:e^-$ (compare Figures 1 and 2). Atomic DOS plots show that *p*-states belonging to Kr and Xe appear deep (~ –5 eV) in the valence band. Charge density plots show that encapsulation resulted in no charge transfer from the lattice to Kr (or Xe).

3.3. Encapsulation of halogen atoms (Br and I)

The encapsulation energies for Br and I are highly negative (favourable) with respect to their isolated atom reference states. This is due to the strong electron affinities of these species (see Table 3), reflected in the negative Bader charges. Both Br and I gain almost one electron

from the extra-framework electrons localised in the one dimensional channel, meaning that both Br and I are tending towards Br^- and I^- respectively, close to completing their p-shells (p^6). The encapsulation energy of Br is more favourable than that of I due to its smaller atomic radius[42]. This is reflected in the shorter bond length of Y-Br than Y-I.

The exothermic endoergic encapsulation energy calculated using $\frac{1}{2}X_2$ (X=Br and I) as the reference indicates that both Br and I are still stable inside $Y_5Si_3{:}e^-$, despite there being an energy penalty to dissociate their diatomic molecules. The calculated dissociation energies (per atom) for Br_2 and I_2 are 1.26 eV and 1.12 eV respectively. Despite the higher dimer dissociation energy for Br than I, Br exhibits a strong encapsulation energy.

Although encapsulation of Br and I results in a reduction of states associated with free anionic electrons at the Fermi level in the total DOS plots, at this concentration of encapsulation, these materials retain their metallic character (see Figure 3). There is, however, an accumulation of charge density around the encapsulated atoms in the one dimensional channel. Encapsulation introduces a slight increase in overall volume. The larger atomic radius of I is reflected in a larger increase in the total volume (see Table 3).

3.4. Encapsulation of a Te atom

Te demonstrates a strong negative (favourable) encapsulation energy (see Table 4). This is due to the transfer of 1.42 electrons to Te. The large Bader charge of 1.42 |e| means that the Te is tending to the stable Te^{2-} ion electronic configuration. A highly exothermic encapsulation energy is also calculated with respect to the dimer, despite the strong Te_2 dissociation energy of 1.46 eV per atom.

At this level of Te encapsulation the material maintains its metallic character (see Figure 4b). That is, free electrons are left in the one-dimensional channel. Though a single Te atom can gain only part of the electron density from the channel, the volume increase for Te is larger than for I, due to the larger size of Te^{2-} than I^-. The accumulation of electrons by the Te is confirmed in the charge density plot where charge density is more localised on the Te than the remaining lattice.

3.5. Encapsulation of Rb and Cs atoms

The relaxed configurations associated with Rb and Cs encapsulation are shown in Figure 5 with the encapsulation energies and the Bader charges reported in Table 5. Both Rb and Cs exhibit positive encapsulation energies (2.28 eV and 2.51 eV respectively). This is due to their low electron affinities and large size. Bader charge analysis shows that both Rb and Cs are polarised with small positive charges (0.29 and 0.01 respectively). While Rb and Cs readily

donate their outmost s^1 electrons to form stable noble gas electronic configurations this is not the case in this electride material as channel space has already accommodated electrons.

The total DOSs calculated for Rb and Cs containing materials remain metallic (see Figure 5). Both total DOS and charge distributions are not significantly altered in either case.

3.6. Encapsulation of dimers (Br_2, I_2 and Te_2)

The relaxed structures of Br_2, I_2 and Te_2 dimers occupying channel positions are shown in Figure 6. The encapsulation energies and Bader charges are reported in Table 6. Encapsulation energies calculated using the molecular reference state predict that the encapsulation is favourable and only slightly less favourable than when these anions are encapsulated as separated species (compare with energies in Tables 3 and 4). The molecular dimer bond lengths inside the channel are significantly longer than their corresponding gas phase dimers (which are 2.31 Å, 2.69 Å and 2.58 Å for Br_2, I_2 and Te_2 respectively). Furthermore, negative Bader charges (see Table 6) on the atoms of dimers confirms the formation of adjacent anion pairs rather than molecules. Nevertheless, this suggests that the electride is capable of accommodating high concentrations of Br and I as anions.

3.7. Kinetics of fission products

The encapsulation of fission products is expected to take place via the surface of the $Y_5Si_3{:}e^-$ with the involvement of kinetic barrier. There is lack of experimental date available on the surface structure of this electride leaving the modelling of surface structures difficult for this electride. Future work should model the surface structures and calculate the activation energies and the diffusion pathways for these fission products.

4. Summary

Atomic scale simulation based on DFT has been used to examine the thermodynamic efficacy of Y_5Si_3 as a filter material to encapsulate volatile fission products. It is found that encapsulation is unfavourable for Kr, Xe, Rb and Cs. Conversely, strong encapsulation energies are predicted for Br, I and Te with significant charge transfer from this electride's confined electrons to the encapsulated species. This results in the formation of stable Br^-, I^- and Te^{2-} anions. Encapsulation of Br_2, I_2 and Te_2 dimers resulted in the dissociation of molecules and the formation of separated anion pairs. In conclusion, Y_3Si_3 electride is a promising filter material to trap Br, I and Te from effluent gases released in the processing of spent nuclear fuel.

Conflicts of interest

The authors declare that there is no competing financial interest.

Acknowledgements

Computational facilities and support were provided by High Performance Computing Centre at Imperial College London.

Data Availability Statement

The data that support the findings of this study are available from the corresponding author upon reasonable request.

References

1 V.M. Erfrmenkov, *IAEA Bull*, **4** 37 (1989).

2 P. A. Baisden and C. E. Atkins-Duffin, in Handbook of Nuclear Chemistry, edited by Attila Vértes, Sándor Nagy, Zoltán Klencsár et al. (Springer US, Boston, MA, 2011), pp. 2797.

3 M.I. Ojovan, W.E. Lee, An Introduction to Nuclear Waste Immobilisation, second ed., Elsevier, Oxford, U.K, 2014.

4 E. D. Collins, G. D. Del Cul, and B. A. Moyer, in Advanced Separation Techniques for Nuclear Fuel Reprocessing and Radioactive Waste Treatment, edited by K. L. Nash and G. J. Lumetta (Woodhead Publishing, 2011), p. 201.

5 C. Corkhill and N. Hyatt, in *Nuclear Waste Management* (IOP Publishing, 2018), p. 1.

6 B. H. Hamling and G. F. Jenkins, *Journal of the Air Pollution Control Association* **7**, 256 (1958).

7 S. Hertz, A. Roberts, and Robley D. Evans, *Proceedings of the Society for Experimental Biology and Medicine* **38** (4), 510 (1938).

8 C. D. Whitney and S. Landsberger, *Journal of Radioanalytical and Nuclear Chemistry* **280**, 281 (2009).

9 K. Knebel, J. Jokiniemi, and P. D. Bottomley, *Journal of Nuclear Science and Technology* **56**, 772 (2019).

10 J. Aaseth, V. M. Nurchi, and O. Andersen, *Biomolecules* **9**, 856 (2019).

11 A. Karhu, (NKSe13) Denmark, 1999.

12 J. Huve, A. Ryzhikov, H. Nouali, V. Lalia, G. Augé, and T. J. Daou, *RSC Advances* **8**, 29248 (2018).

13 D. F. Sava, M. A. Rodriguez, K. W. Chapman, P. J. Chupas, J. A. Greathouse, P. S. Crozier, and T. M. Nenoff, *Journal of the American Chemical Society* **133**, 12398 (2011).

14 B. H. M. Billinge, J. B. Docherty, and M. J. Bevan, *Carbon* **22**, 83 (1984).

15 Richard B. Hahn, Samuel Levin, and Robert L. Friedlander, Journal (American Water Works Association) 50 (11), 1499 (1958).

16 J. L. Dye, *Science* **247**, 663 (1990).

17 A. Ellaboudy, J. L. Dye, and P. B. Smith, *Journal of the American Chemical Society* **105**, 6490 (1983).

18 S. Matsuishi, Y. Toda, M. Miyakawa, K. Hayashi, T. Kamiya, M. Hirano, I. Tanaka, and H. Hosono, *Science* **301**, 626 (2003).

19 J. Wang, K. Hanzawa, H. Hiramatsu, J. Kim, N. Umezawa, K. Iwanaka, T. Tada, and H. Hosono, *Journal of the American Chemical Society* **139**, 15668 (2017).

20 Y. Zhang, Z. Xiao, T. Kamiya, and H. Hosono, *The Journal of Physical Chemistry Letters* **6**, 4966 (2015).

21 K. Lee, S. W. Kim, Y. Toda, S. Matsuishi, and H. Hosono, *Nature* **494**, 336 (2013).

22 T. Tada, S. Takemoto, S. Matsuishi, and H. Hosono, *Inorganic Chemistry* **53**, 10347 (2014).

23 W. Ming, M. Yoon, M.-H. Du, K. Lee, and S. W. Kim, *Journal of the American Chemical Society* **138**, 15336 (2016).

24 Y. Toda, H. Hirayama, N. Kuganathan, A. Torrisi, P. V. Sushko, and H. Hosono, *Nature Communications* **4**, 2378 (2013).
25 M. Kitano, S. Kanbara, Y. Inoue, N. Kuganathan, P. V. Sushko, T. Yokoyama, M. Hara, and H. Hosono, *Nature Communications* **6**, 6731 (2015).
26 N. Kuganathan, H. Hosono, A. L. Shluger, and P. V. Sushko, *Journal of the American Chemical Society* **136**, 2216 (2014).
27 E. Feizi and A. K. Ray, *Journal of Display Technology* **12**, 451 (2016).
28 M. Hara, M. Kitano, and H. Hosono, *ACS Catalysis* **7**, 2313 (2017).
29 N. Kuganathan, A. Chroneos, and R. W. Grimes, *Scientific Reports* **9**, 13612 (2019).
30 N. Kuganathan, R. W. Grimes, and A. Chroneos, *Journal of Applied Physics* **125**, 165103 (2019).
31 F. Hayashi, Y. Tomota, M. Kitano, Y. Toda, T. Yokoyama, and H. Hosono, *Journal of the American Chemical Society* **136**, 11698 (2014).
32 C. Song, J. Sun, S. Qiu, L. Yuan, J. Tu, Y. Torimoto, M. Sadakata, and Q. Li, *Chemistry of Materials* **20**, 3473 (2008).
33 G. Chen, et al., *ACS Applied Materials & Interfaces* **9**, 6666 (2017).
34 J. Wang, L. Li, Z. Shen, P. Guo, M. Li, B. Zhao, L. Fang, and L. Yang, *Materials* **11**, 2462 (2018).
35 Y. Lu, J. Li, T. Tada, Y. Toda, S. Ueda, T. Yokoyama, M. Kitano, and H. Hosono, *Journal of the American Chemical Society* **138**, 3970 (2016).
36 G. Kresse and J. Furthmüller, *Physical Review B* 54, 11169 (1996).
37 P. E. Blöchl, *Physical Review B* 50, 17953 (1994).
38 H. J. Monkhorst and J. D. Pack, *Physical Review B* **13**, 5188 (1976).
39 J. P. Perdew, *International Journal of Quantum Chemistry* **28**, 497 (1985).
40 W. H. Press, S. A. Teukolsky, W. T. Vetterling, and B. P. Flannery, Numerical recipes in C (2nd ed.): the art of scientific computing (Cambridge University Press, 1992).
41 E. Parthe, *Acta Crystallographica* 13, 868 (1960).
42 M. Mantina, A. C. Chamberlin, R. Valero, C. J. Cramer, and D. G. Truhlar, *The Journal of Physical Chemistry A* **113**, 5806 (2009).
43 R. F. W. Bader, *Theoretical Chemistry Accounts* 105, 276 (2001).
44 S. Grimme, J. Antony, S. Ehrlich, and H. Krieg, *The Journal of Chemical Physics* **132**, 154104 (2010).

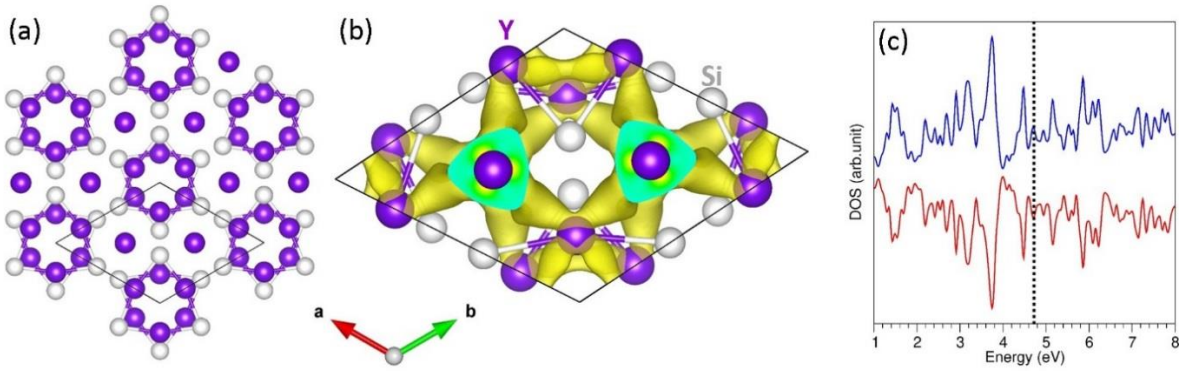

Figure 1. (a) The relaxed structure of bulk $Y_5Si_3:e^-$, (b) one dimensional electrons confined within the crystal and (c) DOS plot of bulk $Y_5Si_3:e^-$. Black dashed lines correspond to the Fermi energy level.

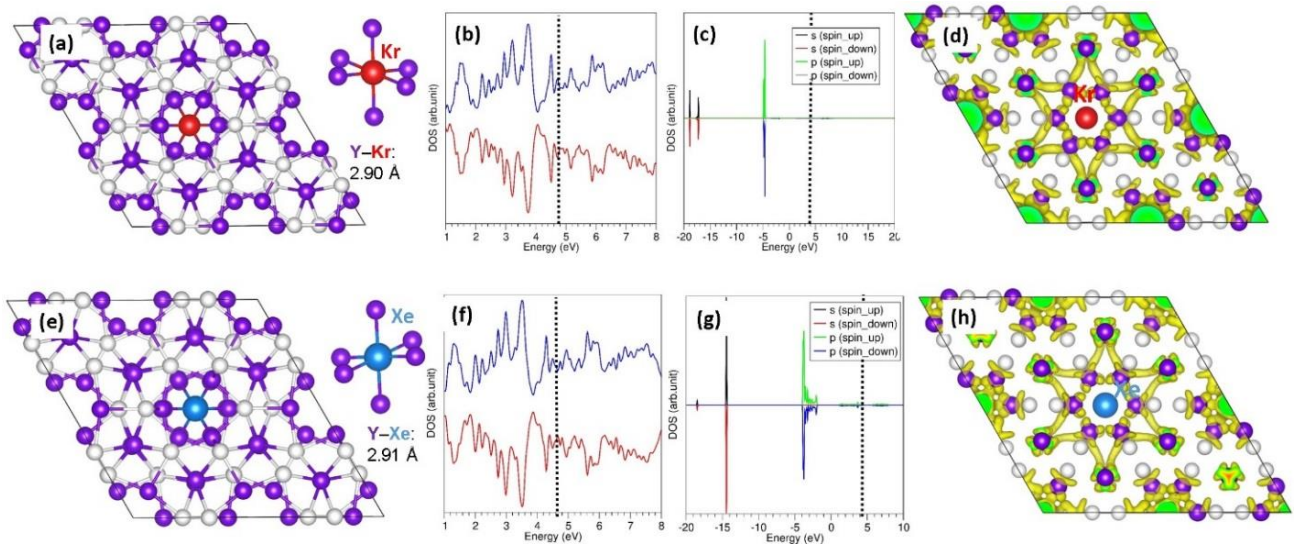

Figure 2. (a) Relaxed structure of Kr encapsulated within $Y_5Si_3:e^-$, (b) total DOS plot (c) atomic DOS plot of Kr (d) constant charge density plot showing electron distribution upon encapsulation and (e-h) corresponding structures and plots calculated for Xe encapsulated within $Y_5Si_3:e^-$.

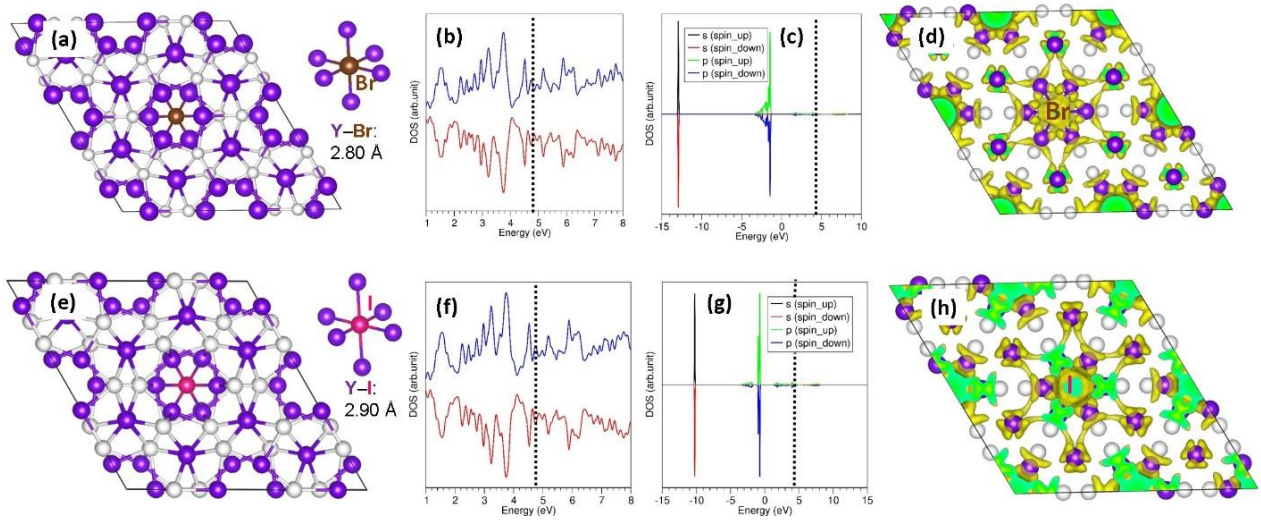

Figure 3. (a) Relaxed structure of Br encapsulated within $Y_5Si_3:e^-$, (b) total DOS plot (c) atomic DOS plot of Br (d) constant charge density plot showing electron distribution upon encapsulation and (e-h) corresponding structures and plots calculated for the I encapsulated $Y_5Si_3:e^-$.

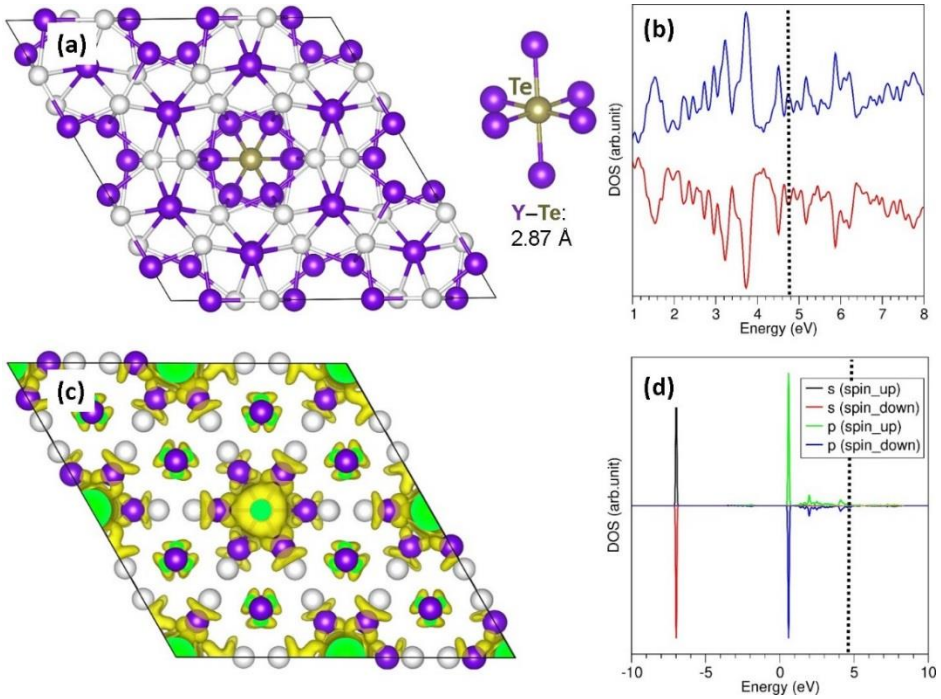

Figure 4. (a) Relaxed structure of Te encapsulated within $Y_5Si_3:e^-$, (b) total DOS plot (c) constant charge density plot showing electron distribution upon encapsulation and (d) atomic DOS plot of Te.

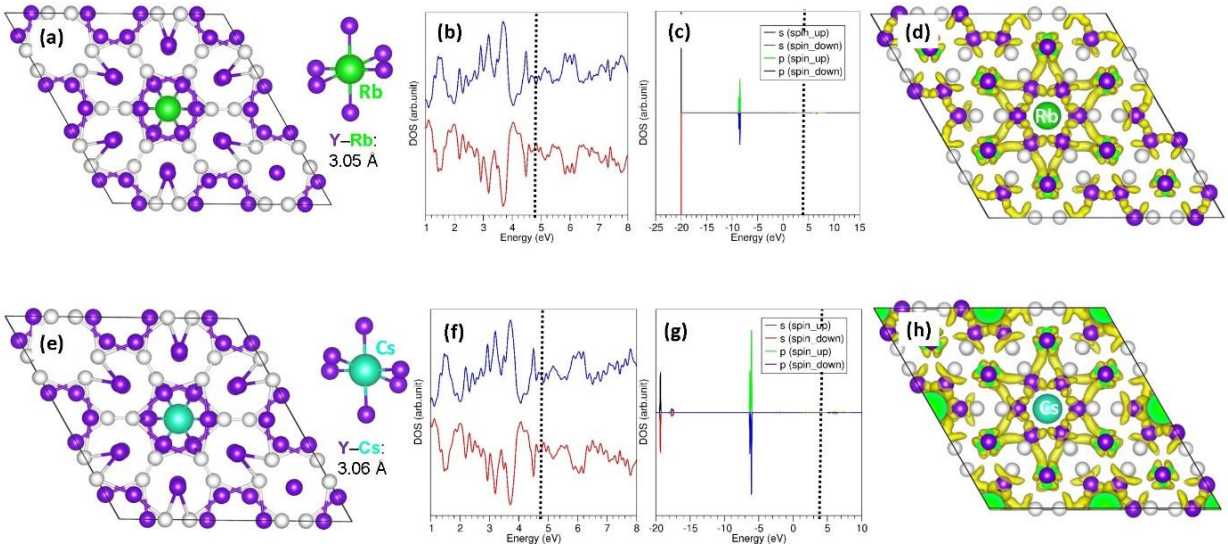

Figure 5. (a) Relaxed structure of Rb encapsulated within $Y_5Si_3:e^-$, (b) total DOS plot (c) atomic DOS plot of Rb (d) constant charge density plot showing electron distribution upon encapsulation and (e-h) corresponding structures and plots calculated for the Cs encapsulated $Y_5Si_3:e^-$.

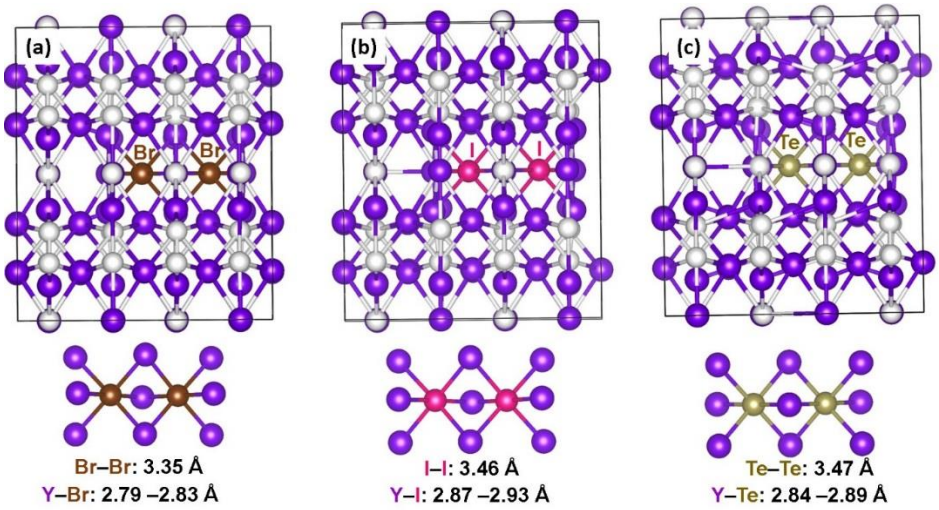

Figure 6. Relaxed structures of (a) Br_2,(b) I_2 and (c) Te_2 encapsulated in $Y_5Si_3:e^-$.

Table 1. Calculated and experimental lattice parameters of the hexagonal crystal structure (space group $P6_3/mcm$) of $Y_5Si_3:e^-$ together with corresponding experimental values.

Parameter	**Calc**	**Expt [41]**	**|Δ|(%)**
a=b (Å)	8.385	8.403	0.21
c (Å)	6.309	6.303	0.09
α = β (°)	90.0	90.0	0.00
γ (°)	120.0	120.0	0.00
V ($Å^3$)	383.96	385.43	0.38

Table 2. Calculated electron affinities of Kr and Xe, encapsulation energies (calculated using the isolated gas phase atom as the reference), Bader charges on the encapsulated atoms, the shortest Y–X bond distances (X= Kr and Xe) and relative volume changes upon encapsulation.

Fission product	Atomic radius (Å)[**42**]	Electron affinity (eV)	Encapsulation energy (eV)	Bader charge (|e|)	Y-X (Å)[X=Kr and Xe]	Relative volume change (Δ%)
Kr	2.02	1.08	2.84	–0.40	2.90	0.62
Xe	2.16	1.24	3.89	–0.48	2.95	0.97

Table 3. Calculated electron affinities of Br and I, encapsulation energies (calculated using the isolated gas phase atoms and dimers as reference states), Bader charges on the encapsulated atoms, the shortest Y–X bond distances (X= Br and I) and relative volume changes upon encapsulation.

Fission product	Atomic radius (Å)[42]	Electron affinity (eV)	Encapsulation energy (eV/atom)		Bader charge (|e|)	Y-X (Å)[X=Br and I]	Relative volume change (%)
			atom	dimer ($\frac{1}{2}$ X_2)			
Br	1.83	4.97	–3.61	–2.35	–1.03	2.80	0.47
I	1.98	4.65	–1.89	–0.77	–1.05	2.90	0.92

Table 4. Calculated electron affinity of Te, encapsulation energy (calculated using the isolated gas phase atom and dimer as reference states), Bader charges on the Te atom, the shortest Y–Te bond distances and relative volume changes upon encapsulation.

Fission product	Atomic radius (Å)[42]	Electron affinity (eV)	Encapsulation energy (eV/atom)		Bader charge (|e|)	Y-Te (Å)	Relative volume change (%)
			atom	dimer ($\frac{1}{2}$ Te_2)			
Te	2.06	3.49	−3.64	−1.88	−1.42	2.87	0.96

Table 5. Calculated electron affinities of Rb and Cs, encapsulation energies (calculated using the isolated gas phase atoms), Bader charges on the encapsulated atoms, the shortest Y–X bond distances (X= Rb and Cs) and relative volume changes upon encapsulation.

Fission product	Atomic radius (Å)[42]	Electron affinity (eV)	Encapsulation energy (eV)	Bader charge (|e|)	Y-X (Å)[X=Rb and Cs]	Relative volume change (%)
Rb	3.03	2.57	2.28	+0.29	3.05	0.93
Cs	3.43	2.22	2.51	+0.01	3.05	0.96

Table 6. Encapsulation energies and Bader charges calculated for dimers encapsulated in $Y_5Si_3:e^-$.

Reaction	Encapsulation energy (eV/atom) with respect to dimer	Bader charges |e|
		On both Br or I or Te atoms
$Br_2 + Y_5Si_3:e^- \rightarrow Br_2\bullet\ Y_5Si_3:e^-$	−2.23	−0.98, −0.97
$I_2 + Y_5Si_3:e^- \rightarrow I_2\bullet\ Y_5Si_3:e^-$	−0.58	−0.98, −0.97
$Te_2 + Y_5Si_3:e^- \rightarrow Te_2\bullet\ Y_5Si_3:e^-$	−1.75	−1.32, −1.31